Flow of a yield-stress fluid over a cavity: Experimental study of the solid–fluid interface

L.-H. Luu, P. Philippe, Guillaume Chambon

Flow of a yield-stress fluid over a cavity: Experimental study of the solid-fluid interface

L. Luu[a], P. Philippe[a], G. Chambon[b]

[a] *IRSTEA, RECOVER, 3275 route de Cézanne, CS 40061, Aix-en-Provence 13182, France.*

[b] *Université Grenoble Alpes, IRSTEA, UR ETGR, 2 rue de la Papeterie, St-Martin-d'Hères 38402, France.*

Abstract

This paper presents an experimental characterization of the flow of an elasto-viscoplastic fluid (Carbopol) over a dead zone constituted of the same material. The studied configuration consists of a closed rectangular channel with a cavity in its base. A curved solid-fluid interface forms into the cavity, separating a yielded flowing layer above from an unyielded dead zone below. The hydrodynamics of the flow is investigated by means of high-resolution optical velocimetry (PIV). We focus in particular on the velocity profiles and shear-rate evolution in a quasi-longitudinal flow domain located around cavity mid-length. Our measurements show a non-monotonous evolution of the shear rate, which increases from zero at the solid-liquid interface, passes through a peak (sometimes leveling off at its maximum value), and returns to zero in a plug zone sufficiently far above the cavity. Two main flow zones can be distinguished: a Poiseuille zone, in which velocity profiles are the same as in the flow over a rigid wall, and a boundary layer ensuring the transition with the dead zone. Hence, consistently with our previous work (*Luu et al., Phys. Rev. E, 2015*), the flow self-organizes to partially smooth out the bottom perturbation. The characteristic thicknesses of the flow zones are shown to evolve with cavity length and hydrodynamic properties of the incoming flow. The study also points out the influence of elastic effects, notably on the shape (asymmetry) of the solid-fluid interface.

Keywords:
Hershel-Bulkley rheology, Elasto-viscoplastic behavior, Solid-fluid transition, Poiseuille flow, Particle image velocimetry

1. Introduction

A large number of materials involved in geophysical or industrial flows present the property to behave either as fluids or solids depending on the applied solicitation: mud, snow, grains, pastes, paints, etc. In many of these complex materials, the solid-fluid transition is governed, at least as a first approximation, by a single stress threshold called yield stress [1, 2, 3]. Existence of this yield threshold gives rise to strong feedbacks between flow dynamics and the state of the material, in the form of co-existing yielded and unyielded regions (where the latter can be either static or mobile) in the flows [4]. Static dead zones close to the solid boundaries form, for instance, in flows down wavy channels [5] or through expansions and contractions [6, 7, 8, 9, 10], in flows around objects [11, 12, 13], and in dip-coating processes [14, 15]. Mobile plugs are encountered in free-surface flows [16, 17, 18, 19, 20] or in flows through conduits [21, 5]. In geophysical context, the solid-fluid transition also plays a crucial role in the initiation of mass flows [22, 23] and in the erosive processes arising during the propagation of these phenomena [24, 25].

In detail, the location of the solid-fluid interfaces, and the characteristics of flow and deformation patterns around them, are strongly connected to the rheological properties of the materials in the vicinity of the yield threshold. Numerical simulations have shown that the shape of the dead zones in expansion-contraction configurations [26, 27] or in lid-driven cavities [28] is affected by the (visco-)elastic strains developing in the yielded regions. Similarly, elasticity and normal stresses are deemed responsible of the occurrence of fore-aft asymmetry in flows of yield-stress materials around objects [12, 13]. When existing, thixotropic properties can also play a strong role on the formation of dead zones. Occurrence of viscosity bifurcation [29], in particular, promotes localization of flows in thin layers called shear bands, while most of the material remains unyielded [30, 31, 32]. Investigating flow characteristics in the vicinity of unyielded zones therefore represents a promising pathway to probe and better understand the solid-fluid transition in yield-stress materials.

Yet, detailed experimental investigations of the velocity field close to solid-fluid interfaces remain rare in the literature. A previous study [6] documented the location of the interface in an expansion-contraction experiment with Carbopol, but did not provide direct measurements of flow dynamics. In a similar configuration, and using an inverse emulsion, other authors [7]

reported on the local velocity field in the flow measured by MRI. They argued that flow in the cavity is structured into a shear band of uniform thickness separating two unyielded zones, one static and one mobile. The shear band was characterized by a quasi-constant shear rate. A similar feature, namely a shear band of quasi-uniform thickness, was observed by PIV during the withdrawal of a plate from a Carbopol bath [14, 15]. On the base of these results, it was suggested that such shear bands constitute a generic feature of the *frustrated* flows developping close to dead zones with yield-stress materials [7]. Since these shear bands are observed even in materials that are *a priori* non-thixotropic, they are presumably of a different nature from the shear bands forming in thixotropic materials, and the mechanisms explaining their formation remain unclear. It shall be noted, however, that velocity measurement resolution in these latter studies is hardly sufficient to ascertain the existence of a constant shear rate in the so-called shear bands. In a recent work [9], we used PIV to monitor (with Carbopol) the velocity field above a dead zone formed in a channel presenting an abrupt contraction, and did not observe any zone of constant shear rate in the flow. Sufficiently far from the solid-fluid interface, the flow structure was identical to that observed in absence of contraction, with a central plug and a sheared layer underneath. The shear rate progressively increased when moving away from the plug, reached a maximum at a certain distance from the dead zone, and then decreased to smoothly reach zero at the solid-fluid interface.

In this context, the objective of the present study is to provide high-resolution experimental data on the flow developping in the immediate vicinity of a solid-fluid interface in a yield-stress material. A specific focus was set on obtaining accurate shear-rate data, from which the existence of shear bands could be clarified. To facilitate comparison with existing results, we chose to work in an expansion-contraction configuration. Compared to our previous study [9], this configuration also presents the advantage to give rise, around the center of the cavity, to a zone where the solid-fluid interface is parallel to channel bottom and the flow is almost longitudinal. Shear rates can be derived relatively accurately in this zone, without the need of differentiating all velocity components or of considering tilted reference frames as in [9].

The paper is structured as follows. Experimental methods are described in section 2. Section 3 provides a global overview of the flow pattern above the cavity, as a preliminary to the quantitative characterization of the flow presented in section 4. Finally, section 5 discusses the main implications of

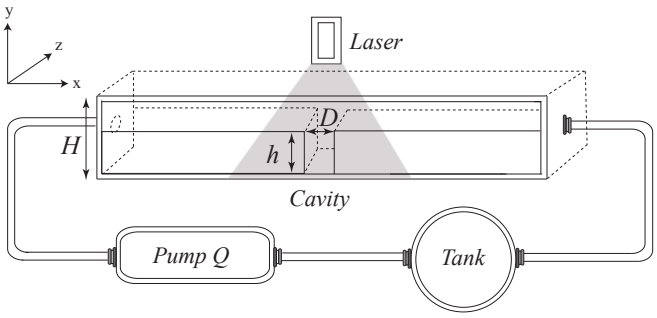

Figure 1: Schematic representation of the experimental setup. Dimensions of the cell are: length 30 cm, height $H = 6.5$ cm, width 8 cm. The cavity of depth h and length D is located in the middle of the cell. Flow rate Q is controlled by a pump in a closed-loop circuit. A vertical laser sheet illuminates the cavity area at half-width of the cell.

our results in relation to previous studies.

2. Experimental setup

2.1. Materials and methods

Our experimental setup is depicted in Figure 1. It consists in a closed parallelepipedic cell with a length of 30 cm (streamwise direction x), a height of $H = 6.5$ cm (crosswise direction y), and a width of 8 cm (spanwise direction z). In the middle of the cell, two steps create a central cavity of length D and height h. To allow for visualization, all the walls of the cell are made of transparent plexiglas. The surface of the steps is roughened to prevent wall slip. Flow rate Q in the cell is imposed by a gear pump, in the range 6.4 – 40.2 cm^3 s^{-1}. Six different cavity configurations were studied, by combining three cavity lengths ($D = 1.5$ cm, 3 cm and 6 cm) and two cavity depths ($h = 1.5$ cm and 3 cm). Note that the thickness $H - h$ of the incoming channel, upwards of the cavity, varied (in the range 3.5 – 5 cm) as cavity depth h was changed. Similarly, the length of the upward channel varied (in the range 12 – 14.25 cm) with cavity length D, but was always sufficient for the incoming flow to be fully established at the entrance of the cavity (see below). Setup geometry is thus completely described by the reduced cavity height $h/(H - h)$ (in the range 0.3 – 0.86) and the reduced cavity length $D/(H - h)$ (in the range 0.3 – 1.7).

As a yield-stress material, we used EDT 2623 Carbopol micro-gel solutions. As illustrated in Figure 2, the steady-state flow curve of this material

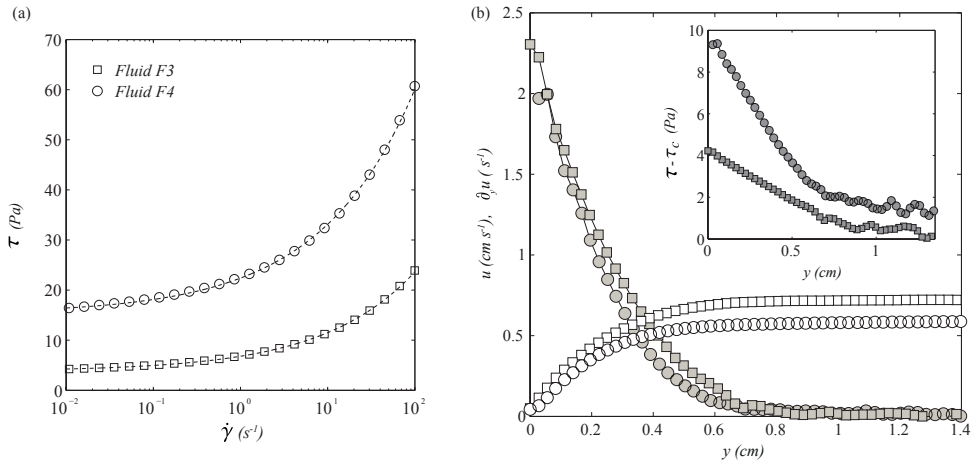

Figure 2: (a) Steady-state flow curves (shear stress τ versus shear rate $\dot{\gamma}$) measured for fluids F3 and F4. Dashed lines correspond to best fits by Herschel-Bulkley (HB) law (parameters are given in Tab. 1). (b) Longitudinal velocity profiles (white symbols) and shear-rate profiles (gray symbols) measured at the entrance of the cavity for fluids F3 and F4 and identical flow rates $Q = 15.3$ cm^3 s^{-1}. Inset: corresponding shear stress profiles computed through HB law [Eq. (1)].

is well represented by a viscoplastic Herschel-Bulkley (HB) constitutive law (for shear rates in the range $10^{-2} - 10^2$ s^{-1}). In simple shear, HB law relates shear stress τ to shear rate $\dot{\gamma}$ according to:

$$\begin{cases} \tau > \tau_c, & \tau = \tau_c + K\dot{\gamma}^n \\ \tau \leq \tau_c, & \dot{\gamma} = 0 \end{cases} \tag{1}$$

where τ_c is the yield stress of the material, K is its consistency, and n is the flow index. Although frequently used as a model viscoplastic material, Carbopol is also known to present more complex rheological trends that are not captured by HB law. In particular, its soft gel-sponge microstructure gives rise to significant visco-elastic properties in solid regime and in unsteady flows [33, 34]. Time effects, such as hysteresis and long transients, have also been described close to flow threshold [35, 36].

Five different Carbopol samples, with different concentrations, were prepared for this study; their rheological characteristics are summarized in Table 1. The density ρ of all samples is equal to 1000 kg m^{-3}. The HB parameters τ_c, K, and n were inferred by fitting the flow curves (Fig. 2a) measured with a parallel-plate laboratory rheometer (using roughened tools to

Fluid	wt (%)	τ_c (Pa)	K (Pa s^n)	n	G (Pa)
F1	0.1	0.2	1.1	0.45	1.9
F2	0.08	0.8	1.4	0.44	6.9
F3	0.1	3.8	3.0	0.41	26.0
F4	0.2	15.3	7.1	0.40	70.4
F5	0.3	21.3	9.6	0.40	87.2

Table 1: Mass concentration, Herschel-Bulkley rheological parameters τ_c, K, n, and elastic shear modulus G, of the five Carbopol samples. Note that samples F1 and F3 result from the same preparation, but F1 was let to age during 3 months, which induced a strong lowering of its HB parameters. Rheometric tests were performed within the week following experiments.

avoid slip). Shear tests consisted in applying progressively decreasing shear-rate values ranging between 10^2 and 10^{-2} s^{-1}, and monitoring the resulting shear stress. Measurement errors on the rheological parameters (determined through systematic repeatability tests) have been evaluated at 10% for τ_c and K, and less than 2% for n [19]. As a minimal characterization of the elastic properties, we also performed oscillatory tests consisting in imposing stress oscillations with a constant amplitude, approximately equal to 10% of τ_c, and a progressively increasing frequency from 1 to 10 Hz. The in-phase component of the strain response exhibits a plateau at large frequencies, from which the elastic shear modulus in solid regime G is derived. No systematic error analysis has been conducted on the values of G, which should therefore be considered only as indicative.

The transparent Carbopol solutions are seeded with 10 μm hollow glass spheres. (Note that the rheometrical tests were performed on samples containing the tracers.) Through illumination by a laser sheet, we could then measure detailed velocity fields in the flow using a particle image velocimetry (PIV) algorithm. Visualization is performed in the longitudinal center-plane of the setup (Fig. 1), where transverse (spanwise) velocities are negligible and the flow can be considered as unaffected by side effects [9]. The velocity field spatial resolution achieved with our setup varied in the range 0.5 – 0.7 mm. Through the dispersion (standard deviation) of data obtained in plug zones where the velocity is expected to remain constant (see below), we estimated a typical velocity measurement error of ± 10 μm s^{-1}. More details concerning the experimental procedures (fluid preparation, rheological characterization, measurement techniques, PIV processing) can be found in [9].

In total, 72 independent experiments were performed for this study. Characteristics of all experiments (fluid, cavity configuration, flow rate) are specified in Appendix A.

2.2. Incoming flow characteristics

The incoming flow, upwards of the cavity, has been studied in detail in [9]. The incoming velocity is purely longitudinal, and velocity profiles in the crosswise direction, $u(y)$, present the typical shape expected for an established Poiseuille flow of a HB fluid (hereafter denoted Poiseuille-HB flow). In particular, a plug zone, where the shear rate is null (and thus u reaches a plateau), is visible in the center of channel, while the shear rate is maximum at the walls. Two examples of such velocity profiles, measured at the entrance of the cavity, are shown in Figure 2b, along with the shear rate $\dot{\gamma} = \partial_y u$ calculated by direct differentiation of the velocity profiles, and the shear stress $\tau = \tau_{xy}$ inferred from Eq. (1). Particularly noteworthy is the linear decrease of the shear stress in the sheared zone, in agreement with Hagen-Poiseuille equation for an established flow (see section 5.1). Quantitatively, we checked in [9] that the measured velocity profiles can be satisfactorily reproduced by the theoretical solutions of this equation (accounting for the independently-determined rheological parameters).

In the following, the experiments are characterized in terms of the non-dimensional Herschel-Bulkley (or Oldroyd) number defined as:

$$Hb = \frac{\tau_c}{K\dot{\Gamma}^n} = \frac{\tau_c}{K}\left(\frac{H-h}{2U}\right)^n, \tag{2}$$

where $\dot{\Gamma} = 2U/(H-h)$ is a characteristic shear rate and U is the maximum velocity (*i.e.* plug velocity) of the incoming Poiseuille-HB flow. We also determined the generalized Reynolds number of the flows:

$$Re = \frac{\rho U^2}{\tau_c + + K\dot{\Gamma}^n}. \tag{3}$$

Values of Hb and Re for all our experiments are indicated in Appendix A. Hb ranged between 0.2 and 5, typically, indicating that both plastic and viscous effects contribute to the flows. Re remained systematically less than 0.12, and less than 0.04 in all but three experiments, indicating essentially inertia-less flows.

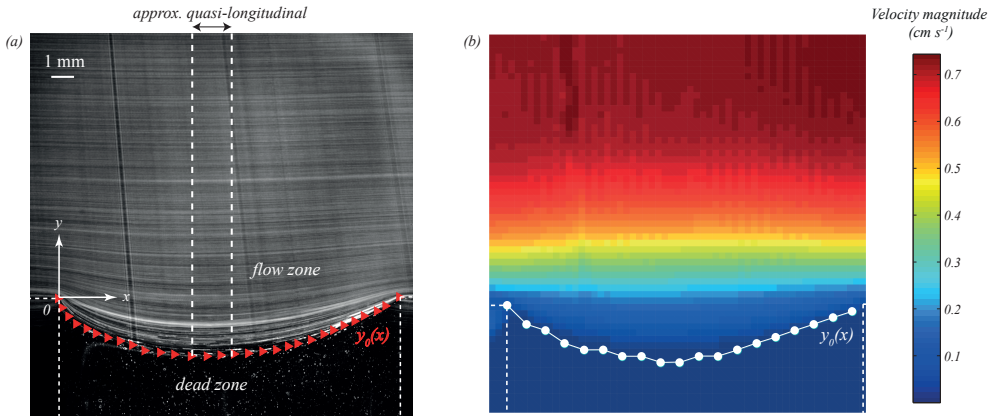

Figure 3: (a) Streamline visualization for sample F3 at a flow rate $Q = 15.3$ cm^3 s^{-1} with cavity length $D = 1.5$ cm and depth $h = 3$ cm. Red triangles delineate the dead zone border recorded by hand on the image (uncertainty is smaller than symbol size). Short-dashed lines represent cavity borders, while long-dashed lines delimit the longitudinal flow domain (see text). (b) Corresponding velocity field (magnitude) obtained by PIV. White circles indicate the zero-velocity isoline.

3. Flow structure above the cavity

3.1. Solid-liquid interface

Figure 3a shows the typical pattern of the streamlines above the cavity, visualized by computing the standard deviation of pixel gray levels over a 1-minute sequence (2723 images). This image clearly highlights the existence of a dead zone in the cavity, in which tracers remain essentially immobile and the material is thus in its solid regime. The dead zone is separated from the flow zone above by a solid-liquid interface, denoted $y_0(x)$, that can be directly delineated on the image (with a typical uncertainty of 0.2 mm). This interface can also be extracted as the zero-velocity isoline in the PIV velocity field (Fig. 3b). Although both methods provide consistent results, the latter generally tends to generate noisier data; we thus chose to base the following analyses on the interfaces recorded with the former method (streamline visualization). Note that coordinate origin is located at the top-left edge of the cavity.

Figures 4 and 5 present the solid-liquid interfaces acquired for the different experiments conducted with fluids F3 and F4, respectively. Apart from peculiar exceptions discussed later (see section 5.4), similar results were obtained

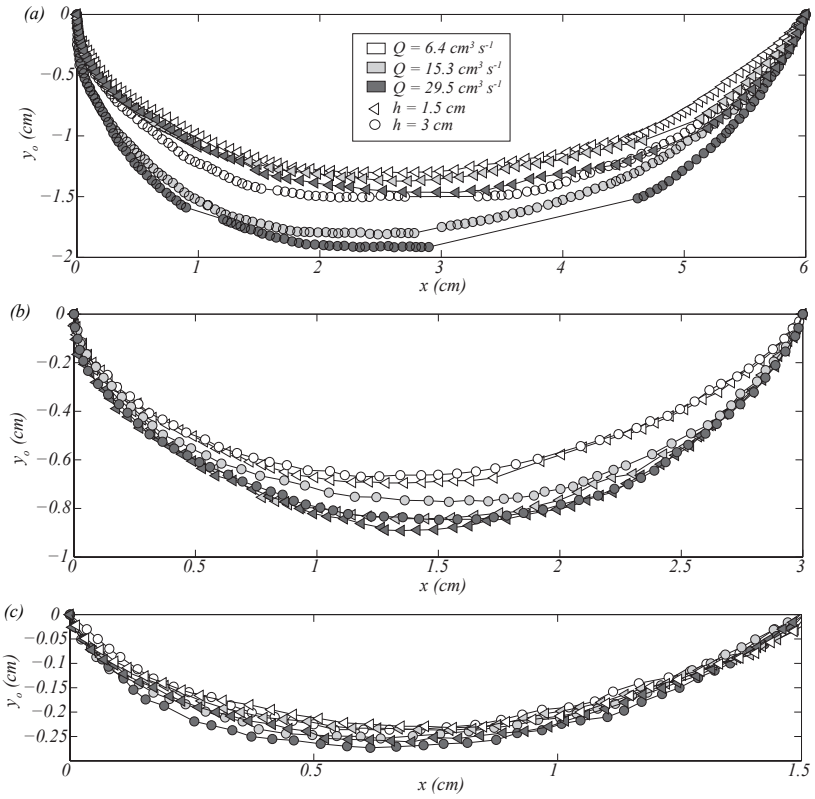

Figure 4: Solid-liquid interfaces recorded for experiments with fluid F3. (a) Results for cavity length $D = 6$ cm. (b) $D = 3$ cm. (c) $D = 1.5$ cm. Legend is common to the three panels.

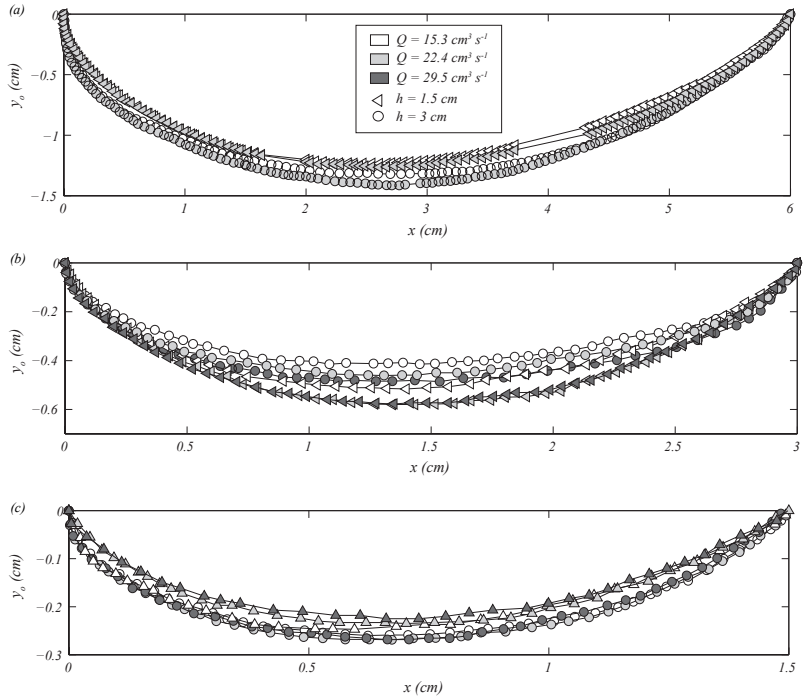

Figure 5: Solid-liquid interfaces recorded for experiments with fluid F4. (a) Results for cavity length $D = 6$ cm. (b) $D = 3$ cm. (c) $D = 1.5$ cm. Legend is common to the three panels.

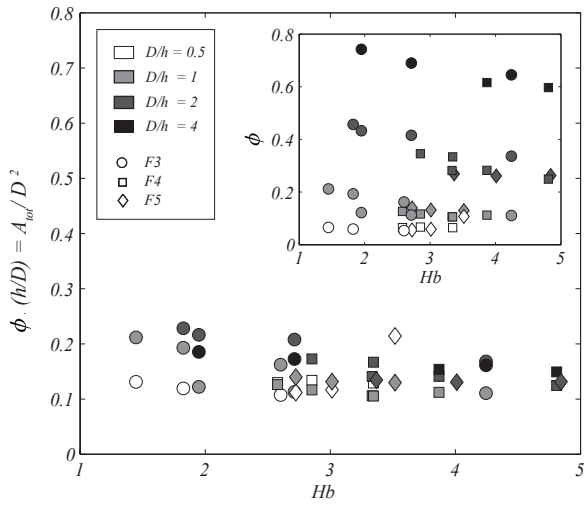

Figure 6: Total yielded area inside the cavity A_{tot} scaled by D^2 as a function of Herschel-Bulkley number Hb for experiments with samples F3, F4, F5. Inset: Displacement efficiency $\Phi = A_{\text{tot}}/(Dh)$ as a function of Hb.

with the other fluid samples. Qualitatively, the interface shape appears to be the same for all flow rates and all cavity dimensions investigated. The interface is always located inside the cavity (negative y_0-values), and with an upside-facing concavity. Maximum interface depth clearly increases when cavity length D increases. For a given value of D, interface depth also tends to increase with flow rate Q. In some cases, however, this latter trend is not obvious since interface position appears to saturate above a certain value of Q (see, *e.g.*, Fig. 5 for $h = 1.5$ cm and the two largest values of Q). Finally, little can be said at this stage concerning the influence of cavity depth h since, as mentioned, changes in h also induce changes in the incoming flow in our experiments.

From the solid-liquid interfaces, the yielded area inside the cavity can be calculated as $A_{\text{tot}} = \int_0^D y_0 dx$. In previous studies [6, 26], this quantity was renormalized by the total cavity area, thereby defining the so-called displacement efficiency $\Phi = A_{\text{tot}}/(Dh)$. As shown in Figure 6 (inset), Φ slightly decreases with the Herschel-Bulkley number of the flow Hb. A strong increase of Φ with cavity aspect ratio, D/h, is also observed. Interestingly, however, Figure 6 (main panel) shows that this influence of D/h is drastically reduced when A_{tot} is renormalized by D^2 instead of Dh. In effect, values of

A_{tot}/D^2 plotted in terms of Hb all roughly collapse on a single, slightly-decreasing, master curve. This indicates that the variations of Φ with D/h are not representative of a "true" physical influence of the aspect ratio on the yielded area, and that the yielded area is essentially independent, at least at first order, of cavity depth h.

3.2. Velocity and shear-rate profiles

In the following, we analyze the velocity field above the cavity by focusing on velocity profiles measured along the crosswise direction y. Figures 7a and 7c show the evolution along the cavity of the longitudinal (u) and vertical (v) velocity profiles for two typical experiments. Longitudinal velocity profiles present a sigmoidal shape, with values of u increasing from 0 at the solid-liquid interface and eventually reaching a plateau in the middle of the channel. As in the incoming flow upwards of the cavity, this plateau is characteristic of the existence of a mobile plug zone. When the solid-liquid interface in the cavity is shallow, *i.e.* for low values of D typically, the longitudinal velocity profiles recorded at different positions x are almost superimposed (Fig. 7a). Consistently, as expected from the continuity condition, vertical velocities remain very small in this case. When the interface is deeper, on the contrary, the different longitudinal velocity profiles along the cavity tend to spread apart (Fig. 7c). Interestingly, however, all the profiles appear to cross at a single position, which roughly corresponds to their inflection point. In this case, vertical velocities are also larger, with maxima located near the edges of the cavity and values that remain close to zero in the center of the cavity. Note also that the plug velocity presents slight variations with x (see insets), meaning that this plug should be considered as a slightly-sheared pseudo-plug rather than as a true plug [37].

Owing to the good accuracy and resolution of our velocity measurements, we could calculate the total shear rate, $\dot{\gamma} = \sqrt{4(\partial_x u)^2 + (\partial_y u + \partial_x v)^2}$, by direct numerical differentiation of the data with a simple finite-difference scheme. As shown in Figures 7b and 7d, the shear rate $\dot{\gamma}$ presents a continuous, non-monotonous evolution starting from 0 in the cavity dead zone and returning to 0 in the upper plug zone, with a maximum in-between. In the shallow-interface case (Fig. 7b), the profiles of $\dot{\gamma}$ display a clearly-peaked shape, with a maximum located near the top of the cavity ($y \approx 0$). This maximum slightly decreases along x until the center of the cavity, where the interface reaches its maximum depth, and then increases again to recover its initial value at the other extremity (Fig. 7b-inset). When the interface

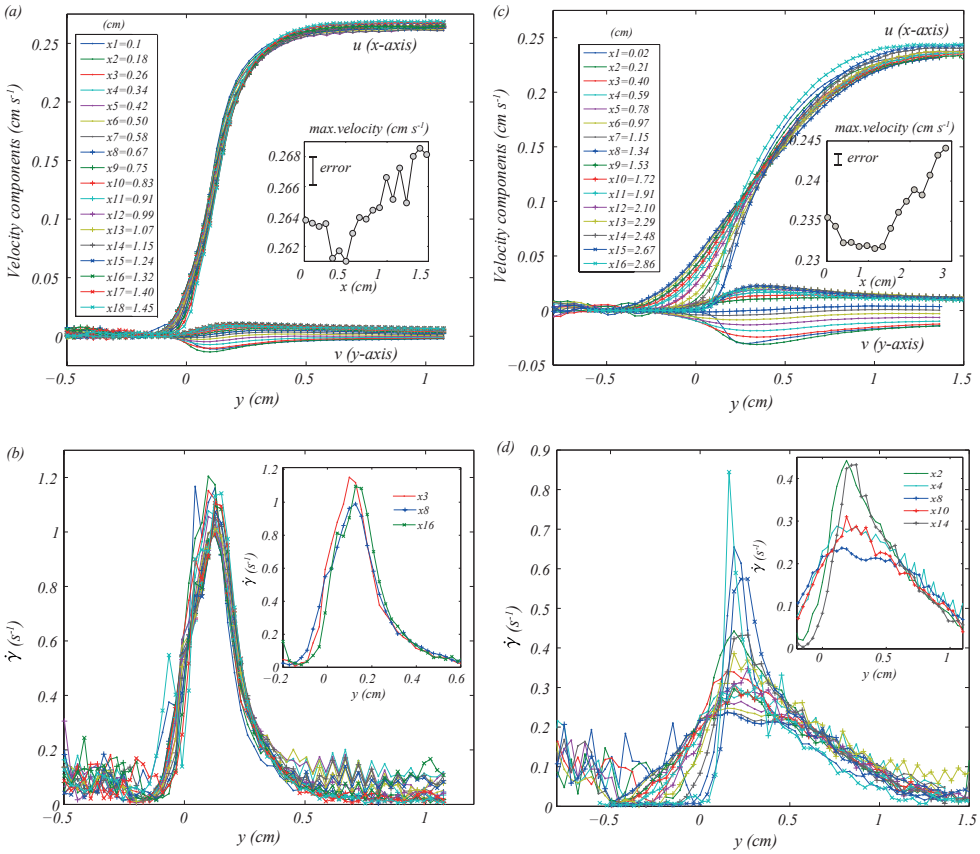

Figure 7: (a) Longitudinal (u) and vertical (v) velocity profiles recorded along the cavity (x-values indicated in legend) for fluid F4 at a flow rate $Q = 15.3$ cm^3 s^{-1} with cavity length $D = 1.5$ cm and depth $h = 1.5$ cm. Inset: evolution along x of the maximum longitudinal velocity, *i.e.* the pseudo-plug velocity. (b) Corresponding shear-rate ($\dot{\gamma}$) profiles. Inset: close-up on the maximum of a few selected profiles. (c) and (d) Idem for fluid F3 at $Q = 6.4$ cm^3 s^{-1} with $D = 3$ cm and $h = 1.5$ cm.

is deeper (Fig. 7d), the profiles of $\dot{\gamma}$ located near the center of the cavity display a qualitatively different shape, with an upper plateau instead of a well-marked peak. The peaked shape remains visible near the cavity edges, and the length of the plateau then progressively increases toward the center of the cavity where it is maximum. The peaks or plateaus are located at an approximately identical position on all profiles, here also close to cavity top, consistent with the common inflection point observed on the velocity profiles.

4. Flow characterization in the vicinity of the solid-fluid interface

4.1. Quasi-longitudinal flow domain

As required by symmetry, flow in the vicinity of the cavity center can be considered as quasi-longitudinal, *i.e.* $v \approx 0$. This property is indeed visible in the streamlines (Fig. 3a) and in the velocity profiles (Figs. 7a and 7c). In this quasi-longitudinal flow domain, the total shear rate can be approximated as $\dot{\gamma} \approx \partial_y u$, which reduces the noise implied by numerical differentiation, and the shear stress can be directly inferred from Eq. (1). All quantities can also be averaged along x, thereby further improving signal-to-noise ratio. In what follows, the detailed quantitative analysis of flow properties in the vicinity of the solid-fluid interface will be restricted to this quasi-longitudinal flow domain. In practice, this domain is defined on the base of a 5% threshold on the standard deviations of longitudinal velocities.

From the typical velocity, shear-rate, and shear-stress profiles obtained in the quasi-longitudinal flow domain, different characteristic positions and flow zones can be defined (Fig. 8). On the left part of the profiles, the position below which velocity and shear rate are null, is denoted y_{int}. This position corresponds to the minimum (*i.e.* maximum depth) of the solid-fluid interface $y_0(x)$. On the other extremity of the profiles, the onset of the plug zone is denoted y_{p}. As expected, shear stress τ approaches the yield stress τ_c at y_{int} and y_p. In-between, the material is in its fluid regime ($\tau > \tau_c$). The flow zone in which shear rate and shear stress decrease is called the Poiseuille-HB (PHB) zone, and its thickness is denoted δ_{PHB}. As explained later (section 5.1), this denomination is motivated by the linear decrease of the shear stress in this zone, exactly as in the incoming Poiseuille-HB flow upwards of the cavity. Conversely, the zone where shear rate and shear stress increase is called the stress-increase (SI) zone, of thickness δ_{SI}. Finally, the thickness of the shear-rate and shear-stress plateaus located at the transition between these two former zones is denoted λ. In practice, and in spite of

the relatively low noise level on the shear-rate data, designing automatic detection criteria for these different zones turned out difficult, such that these zones had to be delimited by hand for each experiment. We considered that the typical uncertainty on the so-determined characteristic thicknesses δ_{PHB}, δ_{SI}, and λ, corresponds to twice the spatial resolution of PIV measurements, *i.e.* ≈ 1 mm. Let us also note that values of λ less than 0.2 cm, typically, denote cases for which the plateaus are actually absent, and for which shear-rate and shear-stress profiles display single peaked maxima.

4.2. Maximum shear stress

Averaging shear-stress values over the plateau zone provides a measure of the maximum shear stress above the cavity τ_m (with an error bar corresponding to the associated standard deviation: see Fig. 8c). The values of τ_m recorded in all our experiments are compiled in Figure 9. A first interesting observation arises when comparing τ_m to the maximum shear stress τ_m^{in} in the incoming Poiseuille-HB flow (measured by extrapolating at the wall the shear stress profiles determined at the entrance of the cavity; see Fig. 2b-inset): as shown in Figure 9a, τ_m is systematically smaller than τ_m^{in}, with a ratio $\tau_m/\tau_m^{\mathrm{in}}$ varying between 0.65 and 0.95 among the experiments. Second, we also notice that when τ_m/τ_c is plotted against the Herschel-Bulkley number Hb (Fig. 9b), all datapoints remarkably collapse on a single master curve. Hence, exactly as the ratio $\tau_m^{\mathrm{in}}/\tau_c$ is directly correlated to Hb in the incoming channel (as expected for an established Poiseuille-HB flow; see Fig. 9b-inset), a univocal relation also seems to exist between τ_m/τ_c and Hb above the cavity.

4.3. Extensions of flow zones

In this section, we summarize the most prominent trends found regarding the extensions of the different flow zones defined above. As shown in Figure 10a, for all the experiments performed, the position of the plug above the cavity, y_p, remains approximately equal to the position of the plug in the incoming Poiseuille flow, y_p^{in}. Accordingly, the shape of this mobile plug is essentially unaffected by the presence of the cavity. Similarly, and although displaying a larger variability, the thickness of the PHB zone δ_{PHB} can also be considered as essentially equal to y_p^{in} in all the experiments (Fig. 10b). This indicates that the lower boundary of the PHB zone always roughly corresponds to the top of the cavity ($y = 0$).

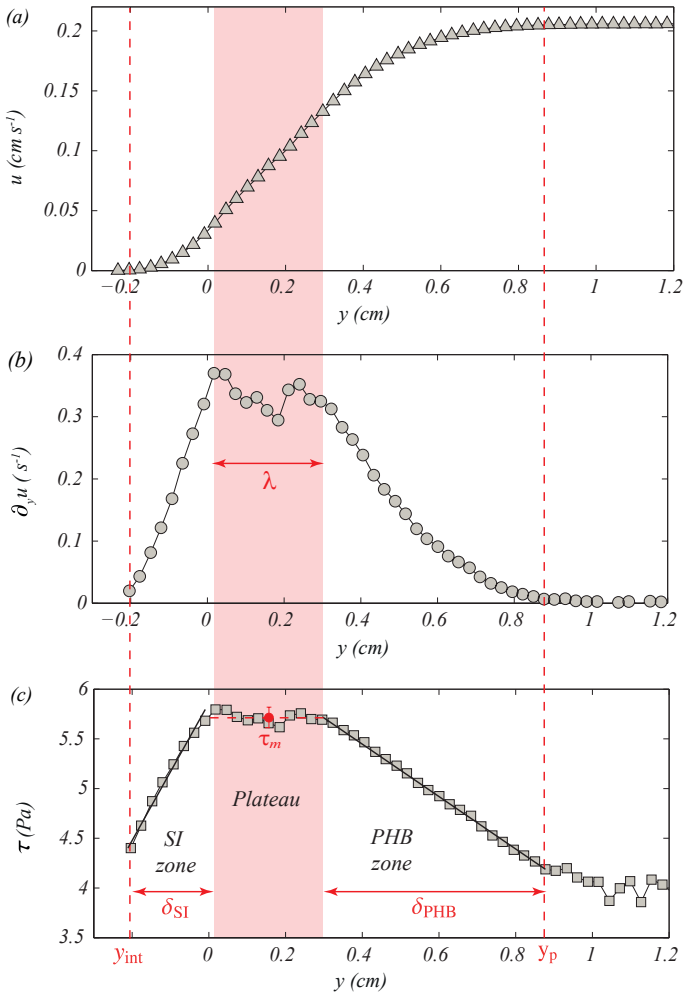

Figure 8: Profiles averaged in the quasi-longitudinal flow domain for fluid F3 at a flow rate $Q = 6.5$ cm^3 s^{-1} with cavity length $D = 1.5$ cm and depth $h = 1.5$ cm. (a) Longitudinal velocity u. (b) Shear rate $\dot{\gamma} = \partial_y u$. (c) Shear stress τ computed through HB law [Eq. (1)]. The different flow zones identified on these profiles (see text) are indicated. The lines in the SI and PHB zones are eyeguides.

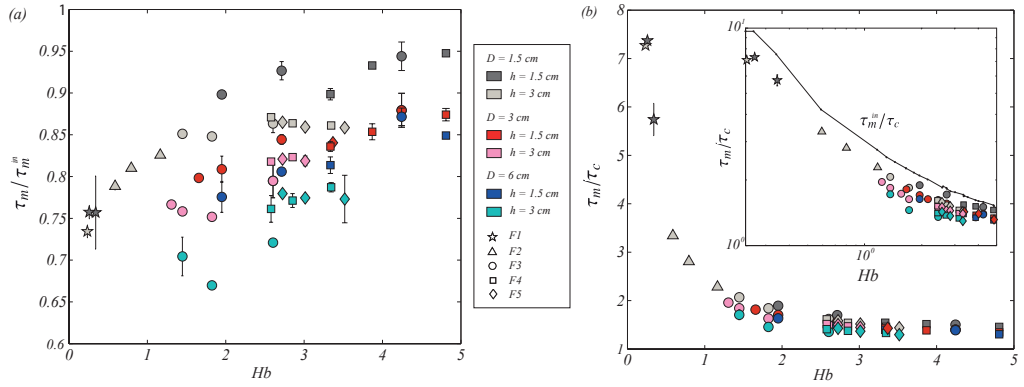

Figure 9: (a) Ratio $\tau_m/\tau_m^{\text{in}}$ between the maximum shear stress above the cavity and the maximum shear stress in the incoming Poiseuille-HB flow, as a function of Herschel-Bulkley number Hb, for all our experiments. (b) Ratio τ_m/τ_c between the maximum shear stress above the cavity and the yield stress as a function of Hb. Inset: same plot in logarithmic scales. The evolution of $\tau_m^{\text{in}}/\tau_c$ versus Hb characterizing the incoming flow is also represented (solid line). In this and the following figures, the different symbols correspond to the different fluid samples, colors identify the different cavity lengths D, and color shades identify the different cavity depths h. When not represented, error bars are smaller than symbol size.

Turning to the thickness of the SI zone, δ_{SI}, we observe that this quantity is mainly controlled by cavity length D and the Herschel-Bulkley number of the flow Hb. As shown in Figure 10c, an approximately unique relation is found between δ_{SI}/D and Hb, indicating that δ_{SI} is actually proportional to D and decreasing with Hb. On the contrary, no similar scaling could be obtained for the thickness of the plateau-zone, λ. Figure 11 shows that, at first order, λ also increases with cavity length D. However, the dispersion of λ-values for each level of D remains large, and no systematic correlations with the Hb number could be found. Notice that, as already indicated, experiments for which the shear-rate profiles display a single peak (no plateau, $\lambda < 0.2$ cm) rather correspond to the lowest value of D. On the contrary, the largest value of D systematically gives rise to a wide plateau. With the intermediate value $D = 3$ cm, both plateau and no-plateau cases have been observed.

4.4. Interface depth

Consistently with previous observations on the solid-fluid interface (Figs. 4 and 5), Figure 12 (inset) shows that the maximum interface depth y_{int} is pri-

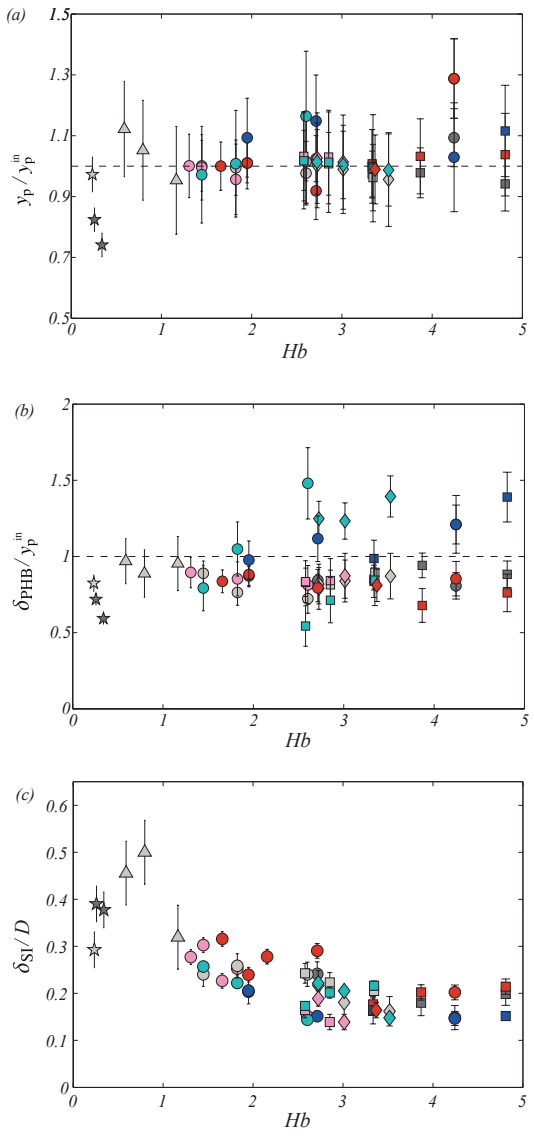

Figure 10: Evolution with Herschel-Bulkley number Hb, for all our experiments, of: (a) plug position y_p normalized by plug position in the incoming flow y_p^{in}; (b) PHB-zone-thickness δ_{PHB} normalized by y_p^{in}; (c) SI-zone-thickness δ_{SI} normalized by cavity length D. Same legend as Fig. 9.

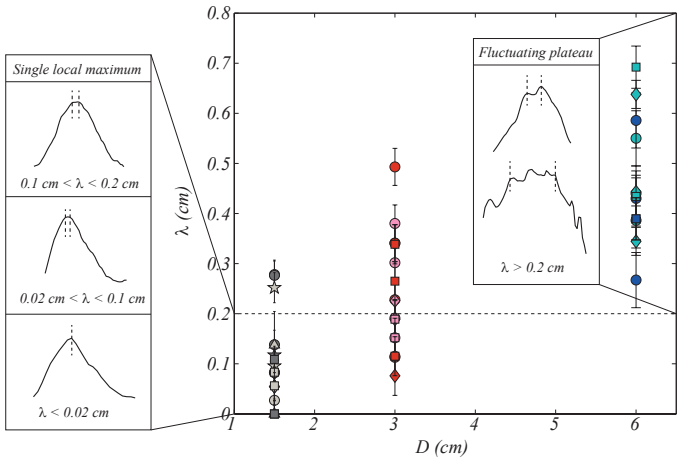

Figure 11: Thickness of shear-rate-plateau λ as a function of cavity length D for all our experiments. The typical morphology of the shear-rate profiles for different values of λ are illustrated in the sub-plots. Same legend as Fig. 9.

marily controlled by cavity length D. An approximately linear decrease of y_{int} (*i.e.* a deepening of the interface) with D is observed. Note that this linear decrease with D is consistent with the scaling of the yielded area A_{tot} by D^2 mentioned previously (Fig. 6b) since, roughly, $A_{\text{tot}} \approx y_{\text{int}} D$. The ratio y_{int}/D is then found to display an increasing trend with the Hb number (Fig. 12, main panel). However, the dispersion of y_{int}/D-versus-Hb datapoints remains relatively large compared to measurement error. We checked whether this variability can be explained by a residual effect of the changes in reduced cavity length $D/(H-h)$ among the experiments (*i.e.* by a slightly non-linear dependence of y_{int} on D). Note that the different colors in Figure 12 actually correspond to different values of $D/(H-h)$. Clearly, no consistent trend with this parameter can be be found. Similarly, we could not find any consistent trend between y_{int}/D and the reduced cavity height $h/(H-h)$. Finally, also noteworthy is the apparent saturation of the ratio y_{int}/D at a value around -0.15. Although experiments involving larger Hb values would probably be needed to confirm this point, we recall that a similar saturation could also be observed in the global interface shapes (Fig. 5).

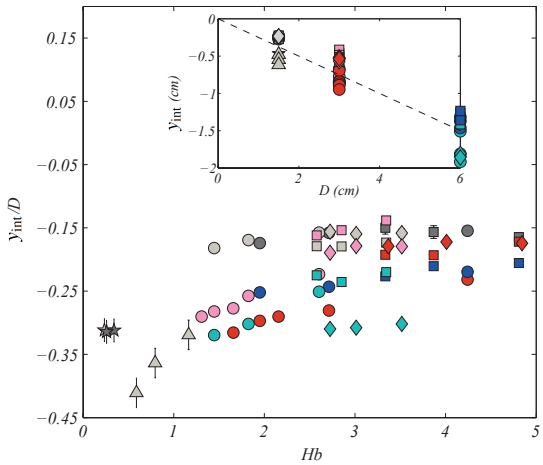

Figure 12: Maximum interface depth y_{int} as a function of Herschel-Bulkley number Hb for all our experiments. Inset: evolution of y_{int} with cavity length D. Same legend as Fig. 9.

5. Discussion

5.1. Poiseuille flow with slip

In the incoming channel upstream of the cavity, the established, purely longitudinal flow, is described by Hagen-Poiseuille equation [21, 9]:

$$0 = -\partial_x p + \partial_y \tau, \tag{4}$$

with $\tau = \tau_{xy}$ the shear stress and p the pressure. The pressure gradient $\partial_x p$ is constant and negative, which leads to a linear decrease of the shear stress τ with y and, therefore, to the classical Poiseuille-HB velocity profile (see Fig. 2b).

An interesting result of our experiments is that, in the range of parameters investigated, this incoming Poiseuille-HB flow is only marginally affected by the presence of the cavity. In particular, the thickness of the plug zone above the cavity remains almost unchanged compared to the upward channel. This observation is in line with previous results from MRI experiments [7] and numerical simulations [5] in which, for similar cavities and hydrodynamic parameters, a constant or modestly-varying plug thickness above the cavity was reported. Our data also reveal that the flowing layer below the plug zone, namely the PHB zone, remains characterized by a linear decrease of the shear

stress with y (Fig. 8c) and, thus, by the same velocity profile as in the upward channel. This Poiseuille-HB velocity profile extends approximately down to $y = 0$, as if the lower wall of the upward channel continued to have a signature even above the cavity. Hence, for the range of parameters tested in our study, everything happens as if the viscoplastic flow self-organized in order to smooth out the existence of the cavity. The only difference between the PHB zone and the flow in the upward channel is the non-zero velocity observed at the lower boundary of the PHB zone. This is due to the requirement of recovering a zero shear rate on the solid-fluid interface below, while the shear rate and shear stress are maximum at the boundary of the PHB zone. To ensure this transition between the PHB zone and the dead zone, a boundary layer, in which shear rate and velocity are increasing with y, forms.

Essentially, the flow above the cavity can thus be described as a Poiseuille-HB flow with apparent basal slip, in agreement with our previous study concerning the flow above a step [9]. Self-organization through formation of dead zones and boundary layers, in order to smooth out perturbations in the boundary conditions, shall thus be regarded as a generic feature of viscoplastic flows. However, and this represents another interesting outcome of the experiments presented here, the relevant parameter controlling the boundary condition at the base of the PHB zone appears to be the shear stress τ_m, rather than the apparent slip velocity itself. This shear stress τ_m is univocally determined by the dynamics of the incoming flow, *via* its Hb number, independently of cavity characteristics (Fig. 9b).

5.2. Fluid mobilization in the cavity

The material in the cavity can be decomposed in a solid fraction (the static dead zone) and a fluid fraction (the above-mentioned boundary layer). The incoming flow thus effectively "mobilizes" part of the material present inside the cavity. The volume of this mobilized fluid (quantified by A_{tot}) or, equivalently, the position of the solid-fluid interface, are primarily controlled by cavity length D: The longer the cavity, the deeper the incoming flow "digs into" the static material. Cavity height h (or, rather, reduced cavity height $h/(H - h)$), on the contrary, does not appear to have an influence on the solid-fluid interface, indicating that the unyielded material in the dead zone only plays the role of a boundary condition for the flow above it. This latter property is indeed expected for a viscoplastic material, as shown, *e.g.*, by the numerical simulations of [5]. Clearly, this property would break down for sufficiently long (or sufficiently shallow) cavities, as soon as the solid-fluid

interface would reach cavity bottom. At this point, the single dead zone would break into two dead zones located near cavity lateral borders, and the configuration would become analogous to the flow above a step previously studied [9]. Lastly, for given cavity characteristics, the mobilized volume inside the cavity slightly decreases with the Hb number of the incoming flow. This trend is also consistent with previous numerical results [6, 26], which showed an increase of displacement efficiency $\Phi = A_{\text{tot}}/(Dh)$ with the non-dimensional incoming wall shear stress or with the non-dimensional incoming velocity.

In the boundary layer above the dead zone, the shear stress increases, from the threshold value τ_c at the solid-liquid interface to the maximum value τ_m at the boundary with the PHB zone (Fig. 8c). According to Eq. (4), this stress increase should be accompanied by a positive pressure gradient, unlike in the PHB zone above where pressure gradient is negative. Such a reversal of the pressure gradient inside the cavity was effectively observed in the numerical simulations of [5] and [10]. Furthermore, the former of these numerical studies also pointed out the existence of significant normal stress gradients in the flow above the cavity, such that Eq. (4) should in fact be replaced by:

$$0 = -\partial_x p + \partial_y \tau + \partial_x \tau_{xx}, \tag{5}$$

even in the quasi-longitudinal zone in the center. Interestingly, as demonstrated in Figure 13, our experimental results fully support this numerical finding when normal stresses in the flow are inferred from measured velocity fields according to: $\tau_{xx} = (\tau_c/\dot{\gamma} + K\dot{\gamma}^{n-1})\ \partial_x u$ [3]. Although the magnitude of normal stress τ_{xx} remains relatively small compared to that of shear stress τ, a clear longitudinal gradient of τ_{xx} is observed in the boundary layer, with positive τ_{xx}-values on the left of the cavity and negative τ_{xx}-values on the right (Fig. 13b). A much noisier field is observed in the PHB zone above, but the sign of the normal stress gradient nevertheless appears to be reversed in this zone. We can thus confirm the mechanism proposed by [5], according to which the existence of the dead zone in the cavity, and of the solid-fluid interface, are enabled by the emergence of normal stress gradients in the flow. Lastly, note that numerical results also showed that $\tau_{xx} \approx -p$ everywhere above the cavity [5], such that Figure 13b may also be regarded as representative of (the opposite of) the pressure gradients in the flow.

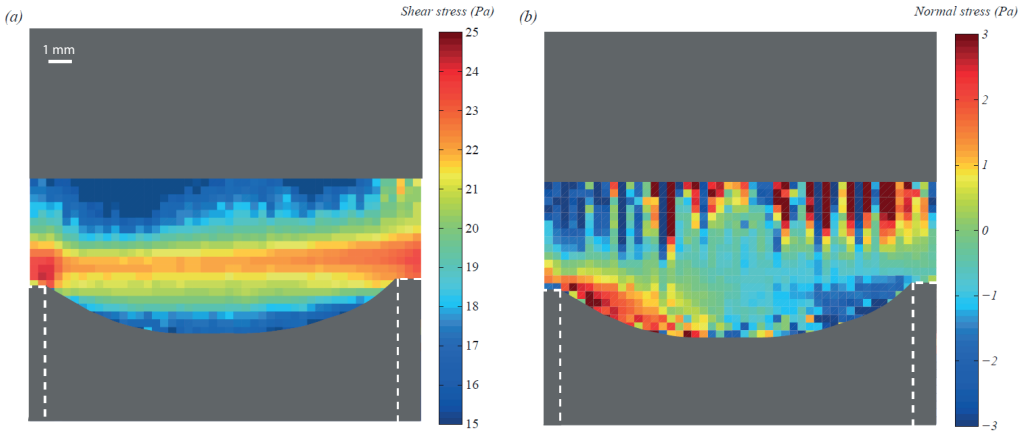

Figure 13: Stress field in the flow above the cavity computed from the tensorial HB law [3] for the same experiment as in Fig. 3. (a) Shear stress $\tau = \tau_{xy}$. (b) Normal stress τ_{xx}. Gray areas mask the unyielded zones in which the stress field cannot be determined. The shape of the upper plug zone is only indicative, as a direct determination from the experimental data turned out very noisy. Dashed lines represent cavity borders.

5.3. Shear band

The observation, above the cavity, of a flowing layer sandwiched between two unyielded zones is consistent with the MRI results of [7]. However, unlike in this former study, our data do not support the description of this flowing layer as a shear band characterized by a constant shear rate and a quasi-uniform thickness. Thanks presumably to a higher measurement resolution, we clearly demonstrate the existence of non-monotonous variations of the shear rate, and of a complex flow structure (PHB zone and boundary layer), above the cavity. Noteworthy, nonetheless, is the existence in some of our experiments of a shear-rate (and shear-stress) plateau that could be reminiscent of such a shear band. When existent, this plateau is part of the boundary layer below the PHB zone, and is characterized by maximum values of shear stress and shear rate. Its width λ is highly variable among the experiments, depending on cavity length D and incoming flow characteristics (Fig. 11). Furthermore, unlike the width of the stress-increase zone δ_{SI}, which is primarily controlled by D and the Hb number of the incoming flow, the width of the plateau λ appears uncorrelated to Hb. We may thus wonder whether the existence and dimensions of this apparent shear band are related

only to the viscoplastic characteristics of the flow, or whether other effects also come into play (see below).

5.4. Beyond viscoplastic effects

Several of the results described above suggest that a purely viscoplastic description may not be sufficient to fully account for our experimental data. First, the variability observed in the location of the solid-fluid interface and, notably, in the values of interface depth y_{int} (Fig. 12). With a viscoplastic fluid, the ratio y_{int}/D would on the contrary be expected to follow consistent trends with Hb for each value of reduced cavity depth $D/(H-h)$, as demonstrated in particular by numerical simulations [10]. Second, the saturation of this same ratio y_{int}/D at a value < 0, whereas, as exemplified again by numerical simulations [10], one would expect the interface depth y_{int} to tend monotonically towards 0 when Hb becomes large. Third, as already mentioned, the absence of correlations between the characteristic width of the shear rate plateau λ and Hb, as a hint that the existence and size of this plateau might be unrelated to viscoplastic effects. All these observations tend to indicate that additional characteristics of the flow, beyond viscoplastic properties, have to be taken into account to fully rationalize the data. Since Carbopol is actually an elasto-viscoplastic material (see section 2.1), with a relatively low ratio G/τ_c and hence a relatively soft character, elasticity appears as a natural candidate to investigate.

A strong argument in favor of the role of elasticity in our results comes from the observation of asymmetry in the flow pattern above the cavity. In particular, as clearly seen in Figure 4, the solid-fluid interface generally displays a slightly asymmetric shape, with the maximum depth shifted towards the left half of the cavity. As the flows are essentially inertia-less, complete fore-aft symmetry would be expected in the case of purely viscoplastic materials [6]. We quantified this asymmetry by computing the difference between the yielded areas on the left and right halves of the cavity, $A_{\text{left}}=\int_0^{D/2} y_0 dx$ and $A_{\text{right}}=\int_{D/2}^{D} y_0 dx$. As shown in Figure 14, this difference is systematically positive and ranges between 2 and 15% of the total yielded area A_{tot}. Similar asymmetric interfaces were observed in the experiments of [6], also with Carbopol, and later attributed to elastic effects (elastic strains stored in the unyielded zone) on the base of numerical simulations [26, 27]. The numerical results also showed that the smaller the ratio G/τ_c, the higher the asymmetry. This latter trend, however, is hardly visible in our results

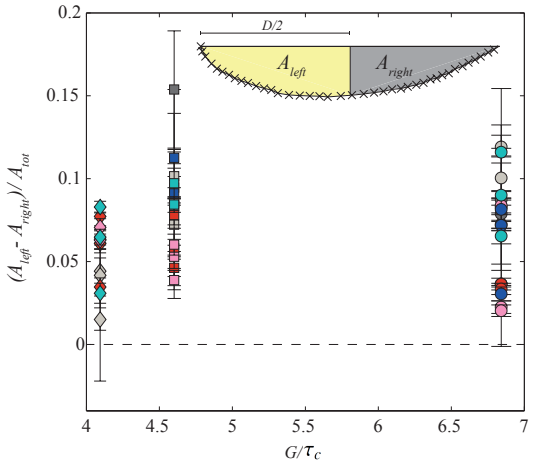

Figure 14: Asymmetry of the solid-fluid interface in the cavity, measured by the quantity $(A_{\text{left}} - A_{\text{right}})/A_{\text{tot}}$ (definition in text), as a function of the ratio G/τ_c for all our experiments. Same legend as Fig. 9.

(Fig. 14), presumably due to experimental noise and a relatively small range of variation of G/τ_c.

Asymmetric features can also be detected in the velocity field above the cavity. The plug velocity, in particular, tends to be slightly higher at the outlet than at the entrance of the cavity (see Figs. 7a and 7c-insets). Here also, existing numerical results indicate that this property could be related to the elasticity of the material [38]. A more recent study [27] also showed, again with numerical simulations, that plug thickness at the outlet of the cavity is reduced, and can even be suppressed, for low enough values of G/τ_c. However, due presumably to the difficulty of properly extracting plug thickness from the experimental data, we were not able to observe this trend in our results.

On the base of these different considerations, it appears plausible that elasticity of the Carbopol samples effectively plays a role in our experiments. The influence of elastic effects can be characterized by the Deborah (or Weissenberg) number defined as:

$$De = \frac{\eta_{\text{eff}}}{G}\frac{U}{D}, \tag{6}$$

with $\eta_{\text{eff}} = \tau_c/\dot{\Gamma} + K\dot{\Gamma}^{n-1}$ the effective viscosity of the material. Typical values

of De range between 6 10^{-2} and 0.9 in our experiments (see Appendix A), indicating that the viscoelastic relaxation time of the material is smaller than, but generally comparable to, the characteristic time D/U of the flow. We were however unable to rationalize further the role of elasticity in our results. In particular, we could not find consistent relations between De and the different characteristic dimensions studied above, notably the interface depth y_{int} or the plateau width λ, nor could we find consistent relations between De and interface asymmetry. As postulated in [12], it is also possible that more complex rheological effects, in particular the development of normal stress differences, come into play. A few existing studies suggest that normal stress differences can be of the same order as shear stresses in Carbopol flows [33], and would therefore need to be better accounted for in the rheological characterization of the material.

To finish, let us mention a peculiar result obtained in some of the experiments conducted with fluid F5, for which the ratio G/τ_c is the lowest. As shown in Figure 15, with this sample, the solid-fluid interface in the cavity does not always present the dug-in, concave shape that is generally observed. In some cases, the interface remains much shallower, close to the top of the cavity, and displays undulations. Strangely, this phenomenon occurs for $D = 1.5$ and 6 cm, but not for $D = 3$ cm. Although, to our knowledge, this phenomenon has never been reported in former experimental or numerical studies involving elasto-viscoplastic materials, we wonder whether it could also be related to elastic effects and, possibly, be the hallmark of an instability of elastic origin. In particular, could this phenomenon be associated to a buckling-like mechanism promoting relaxation of the elastic strains stored in the dead zone? Could it then be related to the apparent saturation of the ratio y_{int}/D pointed out above? (Note that these peculiar interfaces, which correspond to values of y_{int}/D close to 0, were not considered in Fig. 12.) More thorough, dedicated experiments, coupled probably to numerical simulations, would be necessary to precisely assess the occurrence conditions of these undulated interfaces and investigate the underlying mechanisms.

6. Concluding remarks

We presented an experimental study of the flow of a model viscoplastic fluid (Carbopol) over a cavity (expansion-contraction). This configuration was chosen as it is well-suited to investigating flow characteristics in the vicinity of a solid-fluid interface, owing to the formation of an unyielded

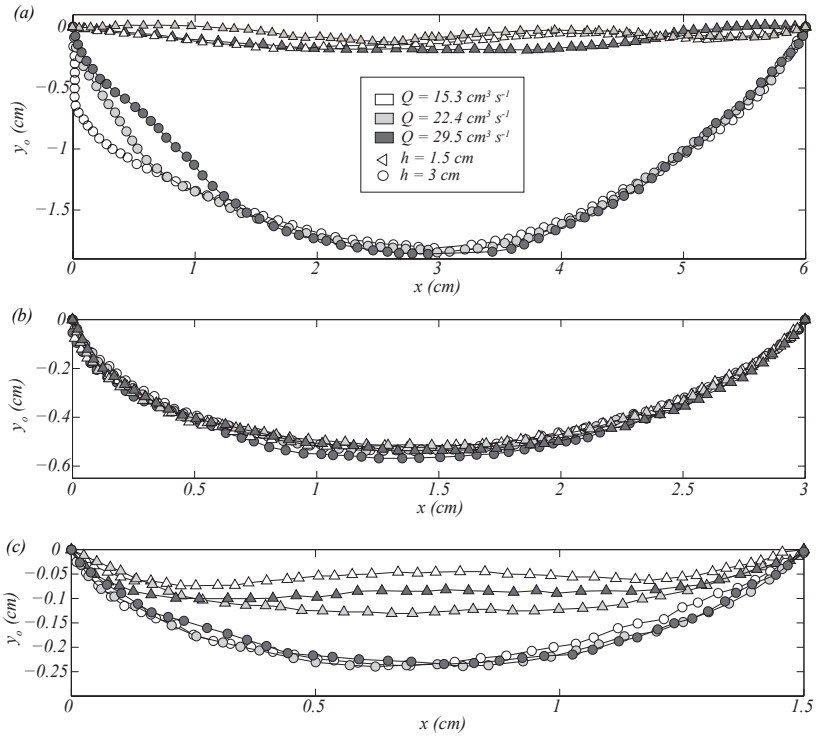

Figure 15: Solid-liquid interfaces recorded for all experiments with fluid F5. (a) Results for cavity length $D = 6$ cm. (b) $D = 3$ cm and (c) $D = 1.5$ cm. Legend is common to the three panels

dead zone inside the cavity. Using high-resolution PIV measurements, our results shed new light on the structure of the flowing layer above the cavity. We showed in particular that a large portion of the layer is characterized by the same Poiseuille-HB velocity profiles as in the incoming channel, as if the existence of the cavity was effectively smoothed out. Below this Poiseuille-HB zone, a boundary layer, in which shear rate and shear stress progressively increase, ensures the transition with the static dead zone. We could also illustrate how the progressive increase of the shear stress when moving away from the dead zone in this boundary layer, is related to the development of significant longitudinal normal stress gradients.

In contrast to what was argued in a few previous studies, our experiments demonstrate that the structure of viscoplastic flows close to solid-fluid interfaces is more complex than a simple shear band characterized by a constant shear rate. Indeed, shear rate and shear stress are not constant in the flowing layer, but present non-monotonous evolutions with well-defined maxima. In some cases, however, a zone of constant shear rate, reminiscent of such a shear band, forms at the lower boundary of the Poiseuille-HB flow zone. The global thickness of the flowing layer ($\delta_{\mathrm{PHB}} + \lambda + \delta_{\mathrm{SI}}$), as well as the position of the solid-fluid interface in the cavity, were shown to vary with both cavity length and the Herschel-Bulkley number Hb comparing plastic and viscous effects. However, more complex rheological properties of Carbopol, as elasticity, are also suspected to play a role on the position of the solid-fluid interface and on the width of the shear-rate plateau λ. The slight asymmetry observed in the shape of the solid-fluid interface, in particular, is known to be a signature of such elastic effects. Yet, the exact mechanisms through which elasticity influences the flow pattern (relaxation effects, strains stored in the unyielded regions, normal stress differences, etc.) remain to be elucidated.

Our high-resolution experimental data now offer a promising benchmark for testing numerical simulation tools developed for yield-stress materials. In particular, the detailed dataset concerning the shape and position of the solid-fluid interface, and the velocity profiles in the boundary layer, shall prove useful to assess the predictive capabilities of numerical schemes based on rigorous treatments of the flow threshold [39, 40, 5, 41, 10]. Comparisons of our results with models implementing elasto-viscoplastic constitutive laws [42, 43, 27] may also help to untangle the respective roles of viscous, plastic and elastic effects, and to better evaluate the influence of elastic effects in Carbopol flows close to the yield threshold. More generally, we argue that the coupling between detailed experimental data and numerical simula-

tions in configurations where flows self-organize into coexisting solid and fluid zones, constitutes a fruitful rheometrical approach to probe the rheological properties of complex fluids in the vicinity of the solid-fluid transition.

Acknowledgments

The authors thank P. Freydier (IRSTEA, ETGR Grenoble) for her help in the rheometrical measurements. The constructive comments of two anonymous referees helped to improve the manuscript. Financial support from CNRS (INSU/INSMI 2016 TELLUS program and INSMI 2017 Défi InFIniTi) is acknowledged. IRSTEA is member of Labex TEC21 (Investissements d'Avenir, grant agreement ANR-11-LABX-0030) and Labex OSUG@2020 (Investissements d'Avenir, grant agreement ANR-10-LABX-0056).

Appendix A. Summary of experiments

Fluid	D	h	Q	Hb	Re	De
F1	1.5	1.5	22.4	0.34	0.012	0.690
			40.2	0.26	0.062	0.854
		3.0	22.4	0.24	0.053	0.646
F2	1.5	3.0	6.4	1.16	$1.6\ 10^{-3}$	0.251
			15.3	0.80	0.018	0.305
			29.5	0.59	0.12	0.365
F3	1.5	1.5	6.4	4.24	$1.9\ 10^{-5}$	0.301
			15.3	2.71	$4.6\ 10^{-4}$	0.333
			22.4	2.16	$2.3\ 10^{-3}$	0.357
			29.5	1.95	$4.6\ 10^{-3}$	0.369
			40.2	1.66	0.014	0.391
		3.0	6.4	2.60	$3.0\ 10^{-4}$	0.236
			15.3	1.82	$3.6\ 10^{-3}$	0.264
			22.4	1.66	$7.1\ 10^{-3}$	0.274
			29.5	1.45	$1.8\ 10^{-3}$	0.288
			40.2	1.31	0.036	0.301
	3.0	1.5	6.4	4.24	$1.9\ 10^{-5}$	0.151
			15.3	2.71	$4.6\ 10^{-4}$	0.167
			22.4	2.16	$2.3\ 10^{-3}$	0.178
			29.5	1.95	$4.6\ 10^{-3}$	0.184

			40.2	1.66	0.014	0.195
		3.0	6.4	2.60	$3.0\ 10^{-4}$	0.118
			15.3	1.82	$3.6\ 10^{-3}$	0.132
			22.4	1.66	$7.1\ 10^{-3}$	0.137
			29.5	1.45	$1.8\ 10^{-3}$	0.144
			40.2	1.31	0.036	0.151
	6.0	1.5	6.4	4.24	$1.9\ 10^{-5}$	0.075
			15.3	2.71	$4.6\ 10^{-4}$	0.083
			22.4	2.16	$2.3\ 10^{-3}$	0.089
			29.5	1.95	$4.6\ 10^{-3}$	0.092
			40.2	1.66	0.014	0.098
		3.0	6.4	2.60	$3.0\ 10^{-4}$	0.059
			15.3	1.82	$3.6\ 10^{-3}$	0.066
			22.4	1.66	$7.1\ 10^{-3}$	0.068
			29.5	1.45	$1.8\ 10^{-3}$	0.072
			40.2	1.31	0.036	0.075
F4	1.5	1.5	15.3	4.81	$8.2\ 10^{-5}$	0.438
			22.4	3.87	$4.0\ 10^{-4}$	0.456
			29.5	3.34	$1.2\ 10^{-3}$	0.471
		3.0	15.3	3.34	$5.7\ 10^{-4}$	0.329
			22.4	2.85	$1.8\ 10^{-3}$	0.342
			29.5	2.58	$3.8\ 10^{-3}$	0.352
	3.0	1.5	15.3	4.81	$8.2\ 10^{-5}$	0.219
			22.4	3.87	$4.0\ 10^{-4}$	0.228
			29.5	3.34	$1.2\ 10^{-3}$	0.235
		3.0	15.3	3.34	$5.7\ 10^{-4}$	0.165
			22.4	2.85	$1.8\ 10^{-3}$	0.171
			29.5	2.58	$3.8\ 10^{-3}$	0.176
	6.0	1.5	15.3	4.81	$8.2\ 10^{-5}$	0.109
			22.4	3.87	$4.0\ 10^{-4}$	0.114
			29.5	3.34	$1.2\ 10^{-3}$	0.118
		3.0	15.3	3.34	$5.7\ 10^{-4}$	0.082
			22.4	2.85	$1.8\ 10^{-3}$	0.086
			29.5	2.58	$3.8\ 10^{-3}$	0.089
F5	1.5	1.5	15.3	4.84	$6.9\ 10^{-5}$	0.491
			22.4	4.01	$2.8\ 10^{-4}$	0.509
			29.5	3.37	$9.9\ 10^{-4}$	0.528

	3.0	15.3	3.52	$3.5\ 10^{-4}$	0.366
		22.4	3.01	$1.1\ 10^{-3}$	0.380
		29.5	2.72	$2.3\ 10^{-3}$	0.390
3.0	1.5	15.3	4.84	$6.9\ 10^{-5}$	0.246
		22.4	4.01	$2.8\ 10^{-4}$	0.254
		29.5	3.37	$9.9\ 10^{-4}$	0.264
	3.0	15.3	3.52	$3.5\ 10^{-4}$	0.183
		22.4	3.01	$1.1\ 10^{-3}$	0.190
		29.5	2.72	$2.3\ 10^{-3}$	0.195
6.0	1.5	15.3	4.84	$6.9\ 10^{-5}$	0.122
		22.4	4.01	$2.8\ 10^{-4}$	0.127
		29.5	3.37	$9.9\ 10^{-4}$	0.132
	3.0	15.3	3.52	$3.5\ 10^{-4}$	0.092
		22.4	3.01	$1.1\ 10^{-3}$	0.095
		29.5	2.72	$2.3\ 10^{-3}$	0.097

Table A.2: Characteristics of all experiments performed: cavity length D (cm), cavity height h (cm), flow rate Q ($cm^3\ s^{-1}$), Herschel-Bulkley number Hb, Reynolds number Re, Deborah number De.

References

[1] C. Ancey, Plasticity and geophysical flows: A review, J. Non-Newton. Fluid 142 (2007) 4–35.

[2] G. Ovarlez, S. Cohen-Addad, K. Krishan, J. Goyon, P. Coussot, On the existence of a simple yield stress fluid behavior, J. Non-Newton. Fluid 193 (2012) 68–79.

[3] N. J. Balmforth, I. A. Frigaard, G. Ovarlez, Yielding to stress: Recent developments in viscoplastic fluid mechanics, Annu. Rev. Fluid Mech. 46 (2014) 121–146.

[4] P. Coussot, Yield stress fluid flow: A review of experimental data, J. Non-Newton. Fluid 211 (2014) 31–49.

[5] A. Roustaei, I. A. Frigaard, The occurrence of fouling layers in the flow of a yield stress fluid along a wavy-walled channel, J. Non-Newton. Fluid 198 (2013) 109–124.

[6] P. R. de Souza Mendes, M. F. Naccache, P. R. Varges, F. H. Marchesini, Flow of viscoplastic liquids through axisymmetric expansions-contractions, J. Non-Newton. Fluid 142 (2007) 207–217.

[7] T. Chevalier, S. Rodts, X. Chateau, J. Boujlel, M. Maillard, P. Coussot, Boundary layer (shear-band) in frustrated viscoplastic flows, Eur. Phys. Lett. 102 (2013) 48002.

[8] T. Chevalier, P. Rodts, C. Chevalier, P. Coussot, Quantitative exploitation of PFG NMR and MRI velocimetry data for the rheological study of yield stress fluid flows at macro and microscales in complex geometries, Exp. Fluids 56 (2015) 1868.

[9] L. H. Luu, P. P., G. Chambon, Experimental study of the solid-liquid interface in a yield-stress fluid flow upstream of a step, Phys. Rev. E 91 (2015) 013013.

[10] P. Marly, P. Vigneaux, Augmented Lagrangian simulations study of yield-stress fluid flows in expansion-contraction and comparisons with physical experiments, J. Non-Newton. Fluid 239 (2017) 35–52.

[11] A. M. V. Putz, T. I. Burghelea, I. A. Frigaard, D. M. Martinez, Settling of an isolated spherical particle in a yield stress shear thinning fluid, Phys. Fluids 20 (2008) 033102.

[12] D. L. Tokpavi, P. Jay, A. Magnin, L. Jossic, Experimental study of the very slow flow of a yield stress fluid around a circular cylinder, J. Non-Newton. Fluid 164 (2009) 35–44.

[13] F. Ahonguio, L. Jossic, A. Magnin, Influence of surface properties on the flow of a yield stress fluid around spheres, J. Non-Newton. Fluid 206 (2014) 57–70.

[14] J. Boujlel, M. Maillard, A. Lindner, G. Ovarlez, X. Chateau, P. Coussot, Boundary layer in pastes – Displacement of a long object through a yield stress fluid, J. Rheol. 56 (2012) 1083–1108.

[15] M. Maillard, J. Boujlel, P. Coussot, Flow characteristics around a plate withdrawn from a bath of yield stress fluid, J. Non-Newton. Fluid 220 (2015) 33–43.

[16] J. M. Piau, Flow of a yield stress fluid in a long domain. Application to flow on an inclined plane, J. Rheol. 40 (4) (1996) 711–723.

[17] G. Chambon, A. Ghemmour, D. Laigle, Gravity-driven surges of a viscoplastic fluid: An experimental study, J. Non-Newton. Fluid 158 (2009) 54–62.

[18] N. Andreini, G. Epely-Chauvin, C. Ancey, Internal dynamics of Newtonian and viscoplastic fluid avalanches down a sloping bed, Phys. Fluids 24 (2012) 053101.

[19] G. Chambon, A. Ghemmour, M. Naaim, Experimental investigation of viscoplastic free-surface flows in steady uniform regime, J. Fluid Mech. 754 (2014) 332–364.

[20] P. Freydier, G. Chambon, M. Naaim, Experimental characterization of velocity fields within the front of viscoplastic surges down an incline, J. Non-Newton. Fluid 240 (2017) 56–69.

[21] J. Peixinho, C. Nouar, C. Desaubry, B. Théron, Laminar transitional and turbulent flow of yield stress fluid in a pipe, J. Non-Newton. Fluid 128 (2005) 172–184.

[22] J. P. Malet, D. Laigle, A. Remaitre, O. Maquaire, Triggering conditions and mobility of debris flows associated to complex earthflows, Geomorphology 66 (2005) 215–235.

[23] G. Mainsant, G. Chambon, D. Jongmans, E. Larose, L. Baillet, Shear-wave-velocity drop prior to clayey mass movement in laboratory flume experiments, Eng. Geol. 192 (2015) 26–32.

[24] R. M. Iverson, Elementary theory of bed-sediment entrainment by debris flows and avalanches, J. Geophys. Res. 117 (2012) F03006.

[25] B. Bates, Fluid dynamics of basal entrainment by geophysical gravity-driven flows, Ph.D. thesis, École Polytechnique Fédérale de Lausanne (2015).

[26] B. Nassar, P. R. de Souza Mendes, M. F. Naccache, Flow of elasto-viscoplastic liquids through an axisymmetric expansion-contraction, J. Non-Newton. Fluid 166 (2011) 386–394.

[27] D. Dall'Onder dos Santos, S. L. Frey, M. F. Naccache, P. R. de Souza Mendes, Flow of elasto-viscoplastic liquids through a planar expansion-contraction, Rheol. Acta 53 (2014) 31–41.

[28] R. Martins, G. M. Furtado, D. D. dos Santos, S. Frey, M. F. Naccache, P. R. de Souza Mendes, Elastic and viscous effects on flow pattern of elasto-viscoplastic fluids in a cavity, Mech. Res. Commun. 53 (2013) 36–42.

[29] P. Coussot, Q. D. Nguyen, H. T. Huynh, D. Bonn, Viscosity bifurcation in thixotropic, yielding fluids, J. Rheol. 46 (2002) 573–589.

[30] P. Coussot, Q. D. Nguyen, H. T. Huynh, D. Bonn, Avalanche behavior in yield stress fluids, Phys. Rev. Lett. 88 (2002) 175501.

[31] H. Tabuteau, F. K. Oppong, J. R. de Bruyn, P. Coussot, Drag on a sphere moving through an aging system, Eur. Phys. Lett. 78 (2007) 68007.

[32] G. Ovarlez, S. Rodts, X. Chateau, P. Coussot, Phenomenology and physical origin of shear localization and shear banding in complex fluids, Rheol. Acta 48 (2009) 831–844.

[33] J.-M. Piau, Carbopol gels: Elastoviscoplastic and slippery glasses made of individual swollen sponges. Meso- and macroscopic properties, constitutive equations and scaling laws, J. Non-Newton. Fluid 144 (2007) 1–29.

[34] L. H. Luu, Y. Forterre, Drop impact of yield-stress fluids, J. Fluid Mech. 632 (2009) 301–327.

[35] A. M. V. Putz, T. I. Burghelea, The solid-fluid transition in a yield stress shear thinning physical gel, Rheol. Acta 48 (2009) 673–689.

[36] T. Divoux, V. Grenard, S. Manneville, Rheological hysteresis in soft glassy materials, Phys. Rev. Lett. 110 (2013) 018304.

[37] N. J. Balmforth, R. V. Craster, A consistent thin-layer theory for Bingham plastics, J. Non-Newton. Fluid 84 (1999) 65–81.

[38] T. Chevalier, Écoulements de fluides à seuil en milieux confinés, Ph.D. thesis, Université Paris-Est (2013).

[39] P. Saramito, N. Roquet, An adaptive finite element method for viscoplastic fluid flows in pipes, Comp. Methods Appl. M. 190 (2001) 5391–5412.

[40] N. Roquet, P. Saramito, An adaptive finite element method for viscoplastic flows in a square pipe with stick-slip at the wall, J. Non-Newton. Fluid 155 (2008) 101–115.

[41] E. D. Fernandez-Nieto, J. M. Gallardo, P. Vigneaux, Efficient numerical schemes for viscoplastic avalanches. Part 1: The 1D case, J. Comput. Phys. 264 (2014) 55–90.

[42] P. Saramito, A new constitutive equation for elastoviscoplastic flows, J. Non-Newton. Fluid 145 (2007) 1–14.

[43] I. Cheddadi, P. Saramito, F. Graner, Steady Couette flow of elastoviscoplastic fluids are nonunique, J. Rheol. 56 (2012) 213–239.